Electro-tunable localized modes in 2D nematic-liquid-crystal photonic crystal with a point defect

Bingxiang Li (李炳祥)[1], Yingmao Xie (谢应茂)[1,2,3*], and Xinghua Wang (王形华)[1,2]

[1] *School of Physics and Electronic Information, Gannan Normal University, Ganzhou 341000, China*

[2] *Institute of Optoelectronic Materials and Technology, Gannan Normal University, Ganzhou 341000, China*

[3] *Key Laboratory of Optoelectronic & Telecommunication of Jiangxi Province, Jiangxi Normal University, Nanchang 330022, China*

[*] *Corresponding author: xieyingmao@126.com*

Received May 8, 2012; accepted June 26, 2012; posted online October 26, 2012

Introducing the finite difference time domain method and perfect match layer absorbing boundary condition, the electro-tunable localized modes in two-dimensional (2D) nematic-liquid-crystal photonic crystal with a point defect (1PD2D-NLCPC) are investigated by numerical simulation. The numerical simulations show that as the direction of the external electrical field varies, the band gap in the 1PD2D-LCPC changes; when the wavelength in the band gap is the wavelength of the sine source wave, the most of optical field energy is localized in the point defect; therefore manipulating the direction of the external electrical field causes the change of the localized mode.

OCIS codes: 160.0160, 160.5298, 350.0350, 350.4238.

doi: 10.3788/COL201210.S21602.

Photonic crystal is a kind of medium in which the refractive index changes periodically[1,2]. With proper designation, there is a band gap in which the propagation of the electromagnetic wave is prohibited. When the photonic crystal has a disorder, the localized mode exists in the photonic crystal band gap[3,4]. Therefore the study of the localized mode is very significant for the resonant micro-cavity. The tunable properties of the band gap arouse more and more researchers' interests[5−10].

It is an economical and functional method for designing photonic crystal that combines the tunable property of the liquid crystal's refractive index with the band gap property of photonic crystal[11−16]. When the electric field intensity is over the threshold, all the directors of the nematic liquid crystal (NLC) parallel the direction of the electric field, that is, the NLC can be considered as a kind of uniaxial material[17]. Therefore, manipulating the direction of the electric field is an easy and feasible way to tune the effective diffraction index of the NLC.

In this letter, we numerically study the electro-tunable properties of the defect mode in the two-dimensional (2D) liquid-crystal photonic crystal with a point defect (1PD2D-LCPC) by the finite difference time domain (FDTD) method and the perfect match layer (PML) boundary condition.

Figure 1 is the structural model of 1PD2D-NLCPC. The gray holes are filled with liquid crystal, while the background is a kind of medium with refraction index of 17. There are 29 rows in this structural model, and the big defect hole locals at the center of the model. The radius of the small hole is 100 nm, and the radius of the big hole is 333 nm. Except the rows where the big defect hole locals, there are 29 small holes at the odd row in the model, while 28 at the even row. The distance of the centers of the two adjacent small holes is 222 nm. In Fig. 1, the black point O is the position of source, and the black points A, B and C are the three detective points. The electric birefringence effect of nematic liquid crystal is shown in Fig. 2, where the direction of the electric field parallels the xoz plane, and θ is the angle between the x axis and the direction of the electric field.

The NLC 4-cyano-4'-pentylbiphenyl (5CB) is introduced for its behavior near the phase transition has been thoroughly studied and its chemical stability against the exposure of strong laser beam[18]. To 5CB, its nematic phase range is from 24° to 35.3°, moreover, its absorption loss can be negligible[19,20]. The permittivity tensor of 5CB can be expressed as

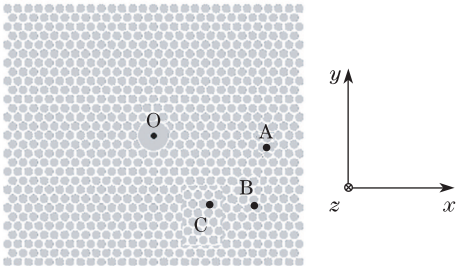

Fig. 1. Structural model of 1PD2D-NLCPC.

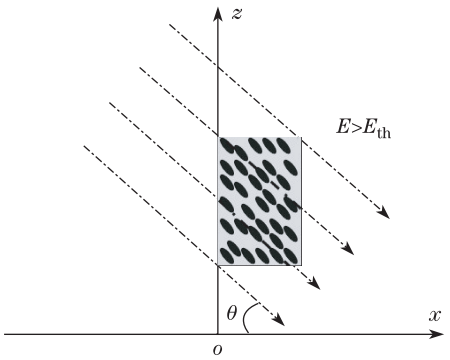

Fig. 2. Electric birefringence effect of nematic liquid crystal.

$$\overline{\overline{\varepsilon'}}=\begin{pmatrix} \varepsilon_{xx}\cos^2\theta+\varepsilon_{zz}\sin^2\theta & 0 & (\varepsilon_{xx}-\varepsilon_{zz})\cos\theta\sin\theta \\ 0 & \varepsilon_{yy} & 0 \\ (\varepsilon_{xx}-\varepsilon zz)\cos\theta\sin\theta & 0 & \varepsilon_{xx}\sin^2\theta+\varepsilon_{zz}\cos^2\theta \end{pmatrix}, \tag{1}$$

where $\varepsilon_{xx}=2.32,\ \varepsilon_{yy}=2.32, \varepsilon_{zz}=2.91$.

The FDTD method and the PML boundary condition are both basing on the maxwell's partial difference equations and introduced to investigate the electromagnetic wave guiding, radiation, and scattering phenomena and technologies[21]. The NLC's parameter tensor can be expressed by Eq. (1) in 1PD2D-NLCPC. The maxwell's curl equations are easy to know as

$$\begin{pmatrix} \frac{\partial H_z}{\partial y}-\frac{\partial H_y}{\partial z} \\ \frac{\partial H_x}{\partial z}-\frac{\partial H_z}{\partial y} \\ \frac{\partial H_y}{\partial x}-\frac{\partial H_x}{\partial y} \end{pmatrix} = \varepsilon_0\overline{\overline{\varepsilon'}}\begin{pmatrix} \frac{\partial E_x}{\partial t} \\ \frac{\partial E_y}{\partial t} \\ \frac{\partial E_z}{\partial t} \end{pmatrix} + \sigma\begin{pmatrix} E_x \\ E_y \\ E_z \end{pmatrix}, \tag{2}$$

$$\begin{pmatrix} \frac{\partial E_z}{\partial y}-\frac{\partial E_y}{\partial z} \\ \frac{\partial E_x}{\partial z}-\frac{\partial E_z}{\partial y} \\ \frac{\partial E_y}{\partial x}-\frac{\partial E_x}{\partial y} \end{pmatrix} = -\mu_0\mu_r\begin{pmatrix} \frac{\partial H_x}{\partial t} \\ \frac{\partial H_y}{\partial t} \\ \frac{\partial H_z}{\partial t} \end{pmatrix} + \sigma_m\begin{pmatrix} H_x \\ H_y \\ H_z \end{pmatrix}, \tag{3}$$

where ε_0 is the free space permittivity (8.85×10^{-12} F/m), $\overline{\overline{\varepsilon'}}$ is the relative permittivity tensor, μ_0 is the free space permeability ($4\pi\times10^{-7}$ H/m), $\mu_{\rm r}$ is the relative permeability which equals 1 in this letter, σ is the electric conductivity which equals 0, σ_m is the equivalent magnetic loss which equals 1, E_x, E_y, E_z and H_x, H_y, H_z are the three components of the electric and magnetic field vector, respectirely.

When it comes to reduction to 2D for transverse magnetic (TM) wave, the spatial derivatives of the electric and magnetic field with respect to Z must equal zero. Under these above conditions, the maxwell's curl equations of TM wave are

$$\begin{aligned} &\frac{\partial H_y}{\partial x}-\frac{\partial H_x}{\partial y} \\ &=\varepsilon_0[\varepsilon_{xx}\sin^2\theta+\varepsilon_{zz}\cos^2\theta \\ &+(\varepsilon_{xx}-\varepsilon_{zz})\cos\theta\sin\theta]\frac{\partial E_z}{\partial t}+\sigma E_z, \end{aligned} \tag{4}$$

$$\frac{\partial E_z}{\partial y}=-\mu_0\mu_r\frac{\partial H_x}{\partial t}-\sigma_m H_x, \tag{5}$$

$$\frac{\partial E_z}{\partial x}=-\mu_0\mu_r\frac{\partial H_y}{\partial t}-\sigma_m H_y. \tag{6}$$

The permittivity and permeability are set as follow in FDTD.

$$\begin{aligned} \varepsilon=&\varepsilon_0[\varepsilon_{xx}\sin^2\theta+\varepsilon_{zz}\cos^2\theta+ \\ &(\varepsilon_{xx}-\varepsilon_{zz})\cos\theta\sin\theta], \end{aligned} \tag{7}$$

$$\mu=\mu_0\mu_r. \tag{8}$$

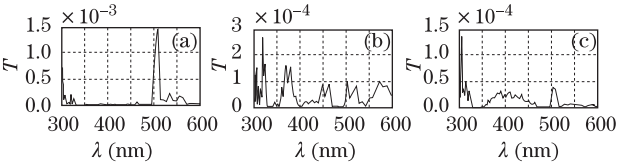

Fig. 3. Spectral plot when $\theta=0°$. (a), (b), and (c) Correspond to the positions A, B, and C in Fig. 1, respectively.

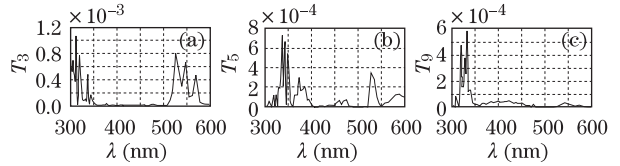

Fig. 4. Spectral plot when $\theta=30°$. (a), (b), and (c) Correspond to the positions A, B, and C in Fig. 1, respectively.

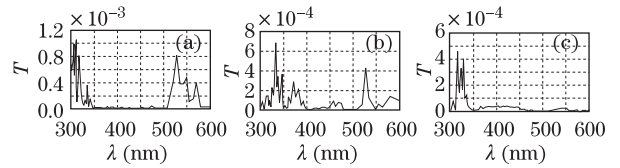

Fig. 5. Spectral plot when $\theta=45°$. (a), (b), and (c) Correspond to the positions A, B, and C in Fig. 1, respectively.

The FDTD method and the PML condition are introduced for numerically simulation. The parameters are set as follow: the size of the computing space is 6.667×6.667 (μm), the time step $\Delta t=9.266\times10^{-18}$ s, the space step $\Delta x=\Delta y=5.556$ nm.

Firstly, for investigating the spectrum properties at the three detective points A, B, and C with the various angles, the modulation Gaussian pulse wave is applied as the wave source. The electric field is set as

$$E_z=\sin(\omega_0 t)\exp\left[-\frac{(t-3\tau)^2}{\tau^2}\right], \tag{9}$$

where t stands for time, and E_z is the electric field intensity of the source at the point O in Fig. 1, the center wavelength of the modulation Gaussian pulses is λ_0=450 nm, $\omega_0=2\pi c/\lambda_0$, the pulse width parameter is $\tau=1.2\times10^{-15}$, the effective calculating wavelength range is from 290 to 610 nm. The ratio of E^2 to $E_z'^2$ at their corresponding frequency obtained after Faster Fourier Transform (FFT) is called as T.

$$T=\frac{E^2}{E_z'^2}. \tag{10}$$

After 25 000 time steps calculation, we acquire the spectral plots of the three detection points with various angles in Figs. 3–7, where θ equals 0°, 3°, 45°, 60°, and 90°, respectively. As is shown in Fig. 3, the range of the band gap's wavelength is from 468.1 to 490 nm when θ equals 0°. In Fig. 4, the range of the band gap's wavelength is from 490.2 to 502 nm when θ equals 30°. In Fig. 5, the range of the band gap's wavelength is from 478.5 to 490 nm when θ equals 45°. In Fig. 60, the range of the band gap's wavelength is from 478.9 to 502 nm when θ equals 60°. In Fig. 7, the range of the band gap's

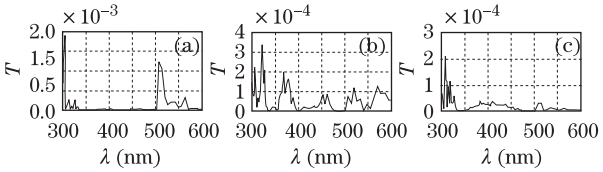

Fig. 6. Spectral plot when $\theta = 60°$. (a), (b), and (c) Correspond to the positions A, B, and C in Fig. 1, respectively.

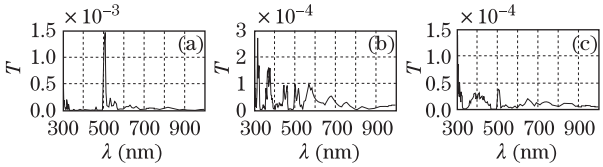

Fig. 7. Spectral plot when $\theta = 90°$. (a), (b), and (c) Correspond to the positions A, B, and C in Fig. 1, respectively.

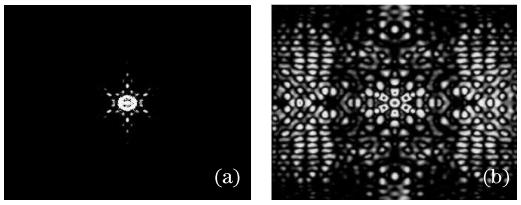

Fig. 8. Optical field distribution when θ=60°. (a) λ=475 nm; (b) λ= 500 nm.

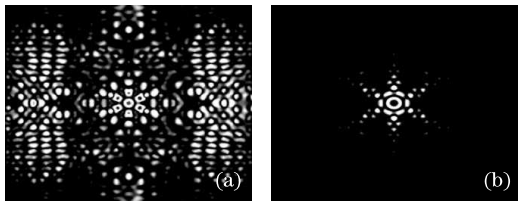

Fig. 9. Optical field distribution when θ=60°. (a) λ=475 nm; (b) λ= 500 nm.

wavelength is from 468.1 to 496.1 nm when θ equals 90°.

Secondly, using the sine wave whose wavelength is 475 or 500 nm as the source wave, we numerically study the optical field distributions when $\theta = 0°$ and 60° in order to obtain the localized property. The optical fields' distributions are obtained in Figs. 8 and 9 after 30 000 time steps calculating. Let $\theta = 0°$, as shown in Fig. 8(a), the most optical field energy is localized in the big defect hole when the wavelength of the wave source λ is 475 nm; as is shown in Fig. 8(b), the optical field energy shows a kind of dispersive distribution in the whole research area when the wavelength of the wave source λ is 500 nm. Let $\theta = 60°$, as shown in Fig. 9(a), the optical field energy shows a kind of dispersive distribution in the whole research area when the wavelength of the wave source λ is 475 nm; as is shown in Fig. 9(b), the most optical field energy is localized in the big defect hole when the wavelength of the wave source λ is 500 nm. The reason of this phenomenon is that the band gap range has changed as the angle θ varies. Therefore, the wavelength in the band gap becomes that outside the band gap, while the wavelength outside the band gap becomes that in the band gap. When the wavelength in the band gap is the wavelength of the sine source wave, the most of optical field energy is localized in the big defect hole, so the band gap is the localized band as well.

In conclusion, after numerically simulating, the electrotunable properties of the localized modes in 2D nematic-liquid-crystal photonic crystal with a point defect are obtained. The structure of the band gap changes as the direction of the electric field changes, the wavelength in the wavelength becomes that outside the band gap, while the band gap outside the band gap becomes that in the band gap. When the wavelength in the band gap is the wavelength of the sine source wave, the most of optical field energy is localized in the big defect hole. So the band gap in this structure is also the localized mode. The investigations of the tunable localized properties are very significant for the 2D resonant cavity and quantum information system.

This work was supported by the National Natural Science Foundation of China under Grant No. 61067002.

References

1. E. Yablonovith, Phys. Rev. Lett. **58,** 2059 (1987).
2. S. John, Phys. Rev. Lett. **58,** 2486 (2010).
3. M. Arka, V. Jelena, and R. Armand, Appl. Phys. Lett. **99,** 251907 (2011).
4. C. Y. Hu, Y.-L. D. HO, D. S. Ivanov E. Engin, M. F. J. Nicol, M. P. C. Tarerne, C. Hu, M. J. Cryan, I. J. Croddock, C. J. Railton, and J. G. Rarity, IEEE J. Quantum Electron. **47,** 1480 (2011).
5. H. W. Yang and D. Xu, Eur. Phys. J. D **64,** 3656 (2011).
6. X. Y. Chew, G. Y. Zhou, F. S. Chau, and J. Deng. IEEE Photon. Technol. Lett. **23,** 1310 (2011).
7. S. K. Yong, S. Y. Lin, S. Y. Wu, and R.-P. Pan, J. Appl. Phys. **109,** 123111 (2011).
8. H. Wang, Y. Luo, Y. Wang, Y. T. Zhang, H.-B. Zhang, and Y.-T. Fang, Physica. B **406,** 2977 (2011).
9. Y. W. Tong and Y. W. Zhang, Phys. Rev. Lett. **86,** 4524 (2001).
10. M. B. Panah, M. S. Abrishamian, and S. A. Mirtaheri, J. Opt. A **13,** 015103 (2011).
11. Y. J. Liu , H. T. Dai, E. S. P. Leong, J. H. Teng, and X. W. Sen, Appl. Phys. B **104,** 659 (2011).
12. L. Lü, G.-J. Ren, B. Liu, and J.-Q. Yao. J. Optoelectr. Adv. Mater. **13,** 755 (2011).
13. C. Y. Liu, Physica E **44,** 313 (2011).
14. J. Cos, J. Ferre-Borrull, J. Pallares, and L. F. Marsal, Opt. Quantum Electron. **42,** 487 (2011).
15. R. Ozaki, H. Moritake, and K. Yoshino, Mol. Cryst. Liq. Cryst. **544,** 77 (2011).
16. M. J. Manzanares and G. P. Castro, J. Electromagn. Waves and Appl. **24,** 1867 (2010).
17. J. A. Reyes, A. J. A. Reyes, and P. Halevi, Opt. Commun. **208,** 2535 (2008).
18. K. Horri and K. Saikai, Phys. Rev. E **73,** 011709 (2006).
19. C. Y. Liu, Y. T. Peng, and J. Z. Wang, Physica B **388,** 124 (2006).
20. G. Ren, P. Shum, and Xi. Yu, Opt. Commun. **281,** 1598 (2008).
21. A. Taflove and S. C. Hagness, *Computational Electrodynamics of the Finite Difference Time Domain Method* (Artech House, Norwood, 2005).